Journal of Catalysis 293 (2012) 195–204

Contents lists available at SciVerse ScienceDirect

Journal of Catalysis

journal homepage: www.elsevier.com/locate/jcat

Shape-dependent interplay between oxygen vacancies and Ag–CeO_2 interaction in Ag/CeO_2 catalysts and their influence on the catalytic activity

Sujie Chang [a,b,c], Mo Li [c], Qing Hua [a,b,c], Lijuan Zhang [d], Yunsheng Ma [c], Bangjiao Ye [d], Weixin Huang [a,b,c,*]

[a] Hefei National Laboratory for Physical Sciences at the Microscale, University of Science and Technology of China, Hefei 230026, China
[b] CAS Key Laboratory of Materials for Energy Conversion, University of Science and Technology of China, Hefei 230026, China
[c] Department of Chemical Physics, University of Science and Technology of China, Hefei 230026, China
[d] Department of Modern Physics, University of Science and Technology of China, Hefei 230026, China

ARTICLE INFO

Article history:
Received 16 May 2012
Revised 28 June 2012
Accepted 30 June 2012
Available online 3 August 2012

Keywords:
Ag/CeO_2 catalysts
CO oxidation
Active structure
Metal–support interaction
Oxygen vacancy
Shape dependence

ABSTRACT

Ag/CeO_2 catalysts employing CeO_2 nanocubes (c-CeO_2) and nanorods (r-CeO_2) as the support were prepared by conventional incipient wetness impregnation followed by calcination at 500 °C in air. Their structures have been characterized in detail and their catalytic activities in CO oxidation have also been tested. c-CeO_2 and r-CeO_2 nanocrystals exhibit different concentrations and structures of oxygen vacancies. The silver-r-CeO_2 interaction is stronger than the silver-c-CeO_2 interaction. Fine Ag nanoparticles form in 1%-Ag/c-CeO_2 and grow in size in 3%-Ag/c-CeO_2; however, positively charged Ag_n^+ clusters dominate in 1%-Ag/r-CeO_2, and fine Ag nanoparticles dominate in 3%-Ag/r-CeO_2. Supported Ag nanoparticles are much more capable of creating oxygen vacancies in CeO_2 than supported positively charged Ag_n^+ clusters. More oxygen vacancies form in Ag/c-CeO_2 than in Ag/r-CeO_2. The average charge density of oxygen vacancies and the ratio between large oxygen vacancy clusters and small vacancies in CeO_2 nanocrystals are enhanced when loaded with positively charged Ag_n^+ clusters but reduced when loaded with Ag nanoparticles. Ag nanoparticles greatly promote the reduction and catalytic activity in CO oxidation of CeO_2 nanocrystals but positively charged Ag_n^+ clusters do not. These results demonstrate the concept that the interplay between oxygen vacancies and Ag–CeO_2 interaction controls the structures of silver and CeO_2 in Ag/CeO_2 catalysts and thus their surface reactivity and catalytic activity, deepening the fundamental understanding of metal/CeO_2 catalysts. These results also reveal that the interplay between oxygen vacancies and Ag–CeO_2 interaction in Ag/CeO_2 catalysts depends on the shape of CeO_2 support, opening up a new strategy for the design of efficient and economic metal/CeO_2 catalysts by engineering the shape of CeO_2 support.

1. Introduction

Oxides are widely employed either as the catalyst or as the support in heterogeneous catalysis. The crystal planes exposed on oxide nanoparticles that determine the surface composition and surface structure have been recognized to remarkably influence their surface reactivity and catalytic performance. Recently, the controlled synthesis of inorganic nanocrystals with a uniform shape that selectively expose one or two types of crystal planes has achieved great progress. Subsequently, it is being developed as a novel strategy to engineer efficient oxide-contained heterogeneous catalysts by controlling the shape of oxide nanocrystals [1]. This novel strategy has been exemplified by shape-dependent surface reactivity and catalysis of MgO [2], Co_3O_4 [3,4], and Cu_2O [5–8] nanocrystals.

Ceria (CeO_2) exhibits a nice Redox property and a high oxygen storage capacity and thus has wide applications in many important catalytic oxidation reactions [9–11]. CeO_2 nanocrystals with various shapes including cubes, rods, wires, and octahedra have been synthesized successfully and examined for catalytic reactions, in which the shape-dependent performance was observed [12–22]. CeO_2 nanorods that predominantly expose {1 1 0} and {1 0 0} crystal planes showed enhanced catalytic activity in CO oxidation than CeO_2 nanoparticles that mainly expose {1 1 1} crystal planes [12]. CeO_2 nanowires that expose a larger portion of {1 1 0} and {1 0 0} crystal planes gave higher oxygen storage capacity and catalytic activity in CO oxidation than CeO_2 nanorods [17]. The metal–CeO_2 interaction plays an important role in the catalytic performance of CeO_2 supported metal catalysts [16,19,20,23–34]. It has also been reported that the shape of CeO_2 nanoparticles strongly affects the metal–CeO_2 interaction and thus the catalytic performance of CeO_2-supported metal catalysts. Among CeO_2 nanorods, nanocubes and nanopolyhedra, CeO_2 nanorods enclosed by {1 1 0} and {1 0 0} crystal planes are most active for gold stabilization/activation and

* Corresponding author at: Department of Chemical Physics, University of Science and Technology of China, Hefei 230026, China. Fax: +86 551 3600437.
E-mail address: huangwx@ustc.edu.cn (W. Huang).

0021-9517/$ - see front matter © 2012 Elsevier Inc. All rights reserved.
http://dx.doi.org/10.1016/j.jcat.2012.06.025

thus CeO_2 nanorod-supported Au catalyst is most active in catalyzing the water–gas shift reaction [16]. The shape effect of CeO_2 nanoparticles on the Au–CeO_2 interaction and catalytic performance of Au/CeO_2 catalysts was also observed in 1,3-butadiene hydrogenation and liquid-phase alcohol oxidation reactions [20]. Feng et al. deposited Pt clusters on CeO_2 nanooctahedra and nanorods employing electron beam evaporation and studied their catalytic activity in CO oxidation and dehydrogenation reaction, in which the growth mode of Pt clusters, Pt–CeO_2 interaction, and catalytic activity of Pt/CeO_2 depended on the shape of CeO_2 nanoparticles [19].

In previous reports [12–20], the shape-dependent catalytic properties of CeO_2 nanocrystals were tentatively attributed to different crystal planes exposed on CeO_2 nanocrystals with different shapes. Theoretical calculation studies showed that CeO_2{1 1 1} is the least active surface, followed by {1 0 0} and {1 1 0} [35]. However, besides the surface composition and surface structure determined by the exposed crystal plane, oxygen vacancies also play a decisive role in the surface reactivity and catalytic performance of CeO_2 nanoparticles [9,10,21,22,36–38] and the concentration and structure of oxygen vacancies have been reported to depend on the preparation process and structure of CeO_2 nanoparticles [21,39,40]. Esch et al. [39] reported that small size surface oxygen vacancies were immobile on CeO_2(1 1 1) at room temperature, but could form linear clusters at high temperatures. Recently, Liu et al. [21] observed that CeO_2 nanorods predominantly exposing less active {1 0 0} and {1 1 1} planes exhibited much better reducibility and catalytic activity in CO oxidation than CeO_2 nanorods predominantly exposing active {1 0 0} and {1 1 0} planes. CeO_2 nanorods predominantly exposing {1 0 0} and {1 1 1} planes were found to have a higher concentration of oxygen vacancy clusters that could promote the reducibility and catalytic activity than CeO_2 nanorods predominantly exposing {1 0 0} and {1 1 0} planes [21]. Theoretical calculation studies show that the vacancy formation energy on different crystal planes CeO_2 follows the order of {1 1 0} < {1 0 0} < {1 1 1} [41]. Wu et al. [42] reported that CeO_2 nanorods with exposed {1 1 0} and {1 0 0} crystal planes have the most abundant oxygen vacancy sites, followed by CeO_2 nanocubes and nano-octahedra, respectively, exposing {1 0 0} and {1 1 1}. The different oxygen vacancy structures in CeO_2 nanorods, nanocubes, and nano-octahedra have also been demonstrated to contribute to their different catalytic activity in CO oxidation [22]. Therefore, Liu et al.'s [21] and Wu et al.'s results [42] reveal that previously reported shape-dependent catalytic activity of CeO_2 nanocrystals in CO oxidation might originate from shape-dependent concentration and structure of oxygen vacancies in CeO_2 nanocrystals.

The shape of CeO_2 nanoparticles has also been reported to strongly affect the metal–CeO_2 interaction and thus the catalytic performance of CeO_2-supported metal catalysts [16,19,20], but the origin remains unknown. In this paper, we employed CeO_2 nanocubes and nanorods as the support to prepare Ag/CeO_2 catalysts. The concentration and structure of oxygen vacancies in CeO_2 and Ag/CeO_2 have been characterized by means of Raman spectroscopy and position annihilation lifetime spectroscopy (PALS) and correlated with the Ag–CeO_2 interaction, reducibility, and catalytic activity of Ag/CeO_2 catalysts. Our results demonstrate that the shape-dependent interplay between oxygen vacancies and Ag–CeO_2 interaction controls the structure and catalytic activity of Ag/CeO_2 catalysts.

2. Experimental section

2.1. Catalyst preparation

$Ce(NO_3)_3{\cdot}6H_2O$ (⩾99.0%), NaOH (⩾96.0%), and $AgNO_3$ (⩾99.8%) were purchased from Sinopharm Chemical Reagent Co., Ltd. and used as received. The synthesis of CeO_2 nanocubes and nanorods followed previously established hydrothermal methods [12]. Typically, 1.96 g $Ce(NO_3)_3{\cdot}6H_2O$ was dissolved in 40 mL ultrapure water (resistance >18 MΩ) and 16.88 g NaOH was dissolved in 30 mL ultrapure water. The NaOH solution was added dropwise into the $Ce(NO_3)_3$ solution under stirring at RT. The mixed solution was adequately stirred for additional 30 min at room temperature and then transferred into a 100-mL Teflon bottle. The Teflon bottle was tightly sealed and hydrothermally treated in a stainless-steel autoclave at 180 °C for 24 h. After cooling, the obtained white precipitate was collected, washed with ultrapure water, and dried in vacuo at 80 °C for 16 h. Then, the acquired yellow powder was calcined in muffle oven at 500 °C for 4 h to synthesize CeO_2 nanocubes. The synthesis procedure for CeO_2 nanorods was the same as that for CeO_2 nanocubes except that the hydrothermal treatment temperature was 100 °C.

Ag/CeO_2 catalysts were prepared by conventional wetness incipient impregnation method employing synthesized CeO_2 nanocubes or nanorods as the support. Typically, 0.5 g CeO_2 nanocrystal was slurried in ultrapure water under vigorous stirring, and the desired amount of $AgNO_3$ solution was added dropwise. After the impregnation, the sample was dried in vacuo at RT and then calcined in air at 500 °C for 4 h. Ag/CeO_2 catalysts with calculated Ag loadings of 1% and 3% (Ag/CeO_2 weight ratio) were prepared and the preparation experiments were carried out in the absence of light.

We herein denote CeO_2 nanocubes and nanorods as *c*-CeO_2 and *r*-CeO_2, respectively, and various Ag/CeO_2 catalysts as 1%-Ag/*c*-CeO_2, 3%-Ag/*c*-CeO_2, 1%-Ag/*r*-CeO_2, and 3%-Ag/*r*-CeO_2.

2.2. Structural characterization

The loading of Ag in Ag/CeO_2 catalysts was determined by an Optima 7300 DV inductively coupled plasma atomic emission spectrometer (ICP-AES). BET specific surface areas were acquired on a Beckman Coulter SA3100 surface area analyzer, and the sample was degassed at 300 °C for 5 h in the nitrogen atmosphere before the measurement. Powder X-ray diffraction patterns were recorded on a MXPAHF X'Pert PRO diffractometer using nickle-filtered Cu Kα (wavelength: 0.15418 nm) radiation source with the operation voltage and operation current being 30 kV and 160 mA, respectively. UV–Vis diffuse reflectance spectra (DRS) were recorded on a Shimadzu SolidSpec-3700 UV–Vis spectrophotometer. X-ray photoelectron spectroscopy (XPS) measurements were performed on an ESCALAB 250 high-performance electron spectrometer using monochromatized Al Kα ($h\nu$ = 1486.7 eV) as the excitation source. The likely charging of samples was corrected by setting the binding energy of the adventitious carbon (C 1s) to 284.8 eV. Laser Raman spectra were obtained in back-scattering configuration on a LABRAM-HR Confocal Laser Raman Spectrometer. The Ar+ (514.5 nm) and He–Cd lasers (325 nm) were respectively employed as the excitation source to obtain the visible Raman and UV Raman spectra. The integration time was 60 and 120 s for the visible and UV Raman spectra, respectively. Transmission electron microscopy (TEM) and high-resolution transmission electron microscopy (HRTEM) experiments were preformed on JEOL-2100F with electron acceleration energy of 200 kV. H_2 temperature-programmed reduction (H_2-TPR) experiments were carried out on a Micromeritics ChemiSorb 2750, in which 20 mg catalyst was heated at a heating rate of 10 °C min^{-1} in a 5% H_2–Ar mixture with a flow rate of 20 mL min^{-1}. X-ray absorption spectra (XAS) were recorded at room temperature in the fluorescence mode at BL14W1beamline of Shanghai Synchrotron Radiation Facility (SSRF), China.

PALS spectra were measured with a fast–fast coincidence spectrometer with a time resolution of 215 ps acquired using silicon single crystal as the reference. The time channel width of our PALS

spectrum measuring system reaches 23.8 ps. Samples were pressed into pellets (1 mm thickness and 10 mm diameter) for PALS measurements. A 40 μCi ^{22}Na positron source was sandwiched between two identical plane-faced pellets. All measurements were carried out at 291 K. The lifetime spectra were best fitted to three lifetime components using the PATFIT program, and the counts of every spectrum were 2.0×10^6.

2.3. Catalytic activity test

The catalytic activity of CeO_2 and Ag/CeO_2 catalysts in CO oxidation was evaluated with a fixed-bed flow reactor. The catalyst experienced no pretreatment prior to the catalytic reaction. The used catalyst weight was 100 mg, and the reaction gas consisting of 1% CO in dry air was fed at a flow rate of 20 mL min^{-1}. The composition of the effluent gas was detected by an online GC-14C gas chromatograph equipped with a TDX-01 column (T = 80 °C, H_2 as the carrier gas at a flow rate of 30 mL min^{-1}). The conversion of CO was calculated from the change of CO concentrations in the inlet and outlet gases. It was confirmed that the investigated catalytic reactions do not have mass and heat transfer limitations [43].

3. Results and discussion

Fig. 1 shows TEM and HRTEM images of as-synthesized CeO_2 nanocubes and nanorods. CeO_2 nanocubes are uniform with their edge lengths mostly between 20 and 30 nm, and CeO_2 nanorods are with a narrow diameter distribution of 10 ± 3 nm but a wide length distribution between 30 and 200 nm. As reported previously [13] and revealed by HRTEM images, CeO_2 nanocubes selectively expose {100} crystal planes and CeO_2 nanorods expose {100} and {110} crystal planes. CeO_2(100) is a polar plane composed of Ce(IV) layers and O layers, and its surface is terminated by the O layer, whereas CeO_2(110) is a non-polar plane formed by a stack of stoichiometric CeO_2 layers and its surface exposes both Ce(IV) and O atoms [41].

Fig. 2 shows XRD patterns of CeO_2 and Ag/CeO_2 samples accompanied with their photographs. Both CeO_2 nanocubes and nanorods display typical cubic fluoride CeO_2 crystal phase (JCPDS card No. 34-0394), but the diffraction peaks of CeO_2 nanorods are slightly broader than those of CeO_2 nanocubes. The colors of CeO_2 nanocubes and nanorods are yellow, and CeO_2 nanorods look slightly brighter than CeO_2 nanocubes. However, after the loading of silver, the colors of the samples vary much. 1%-Ag/c-CeO_2 and 3%-Ag/c-CeO_2 are black, but 1%-Ag/r-CeO_2 is dark yellow and 3%-Ag/r-CeO_2 is black. XRD does not detect any diffraction patterns arising from Ag in 1%-Ag/c-CeO_2, 1%-Ag/r-CeO_2 and 3%-Ag/r-CeO_2, but very weak Ag(111) diffraction peak at 38.6° in 3%-Ag/c-CeO_2, evidencing the presence of Ag nanoparticles in 3%-Ag/c-CeO_2. We measured the silver loading in Ag/CeO_2 samples by ICP-AES, and the results are summarized in Table 1. 1%-Ag/c-CeO_2 and 1%-Ag/r-CeO_2 have similar silver loadings, so do 3%-Ag/c-CeO_2 and 3%-Ag/r-CeO_2. It can be thus inferred that silver species with different structures form in different Ag/CeO_2 samples.

We examined the morphology and structure of Ag/CeO_2 samples with TEM (Fig. 3). The morphology of both CeO_2 nanocubes and nanorods does not change much after the loading of silver; however, their surface becomes rougher and their corners become rounder. We failed to observe any Ag nanoparticles in 1%-Ag/r-CeO_2. Hemispherical Ag nanoparticles, spherical Ag nanoparticles, and both hemispheric and spherical Ag nanoparticles could be observed in 1%-Ag/c-CeO_2, 3%-Ag/r-CeO_2, and 3%-Ag/c-CeO_2, respectively, as evidenced by their lattice fringe of 0.24 nm corresponding to that of Ag{111}. The average size of observed Ag nanoparticles in 3%-Ag/c-CeO_2 is largest, agreeing with above XRD results.

Fig. 4 shows UV–Vis DRS spectra of CeO_2 and Ag/CeO_2 samples. The UV–Vis DRS spectra of CeO_2 nanocubes and nanorods are similar, but CeO_2 nanocubes exhibit slightly stronger absorbance in the visible region than CeO_2 nanorods. The loading of silver greatly enhances the absorbance of CeO_2 in the visible light region, but the enhancement effect is much lower in 1%-Ag/r-CeO_2 than in other three Ag/CeO_2 samples. These experimental results well explain the colors of Ag/CeO_2 samples shown in Fig. 2. Meanwhile, no new feature could be observed in the UV–Vis DRS spectrum of 1%-Ag/r-CeO_2, but a diffuse but clearly visible peak was observed in the UV–Vis DRS spectra of 1%-Ag/c-CeO_2, 3%-Ag/r-CeO_2, and 3%-Ag/c-CeO_2, respectively, centering at 676, 642, and 809 nm. This feature can be reasonably assigned to the surface plasmon resonance (SPR) peak of Ag nanoparticles supported on CeO_2. The SPR peak of Ag nanoparticles red-shifts with their particle size

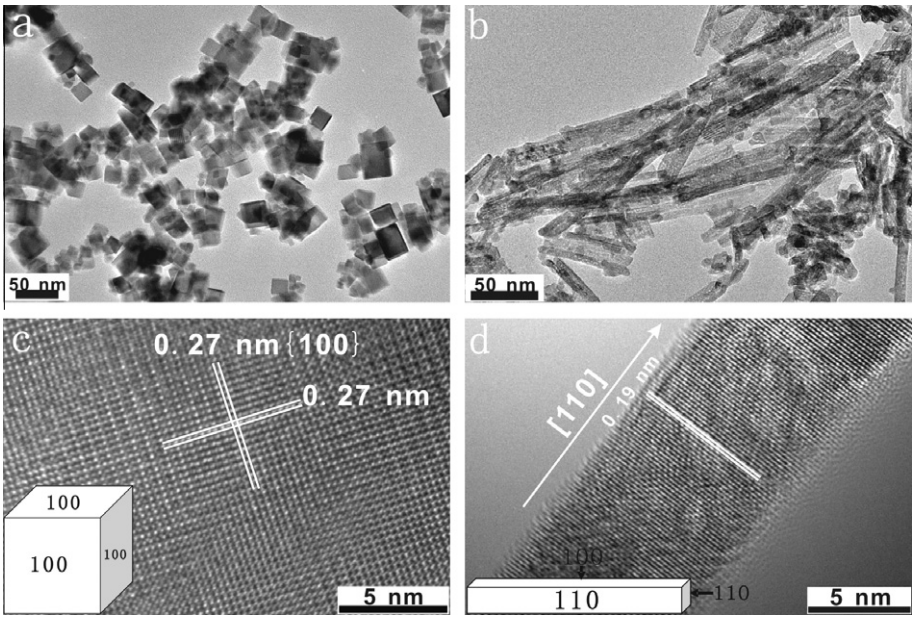

Fig. 1. TEM and HRTEM images of CeO_2 nanocubes (a and c) and nanorods (b and d).

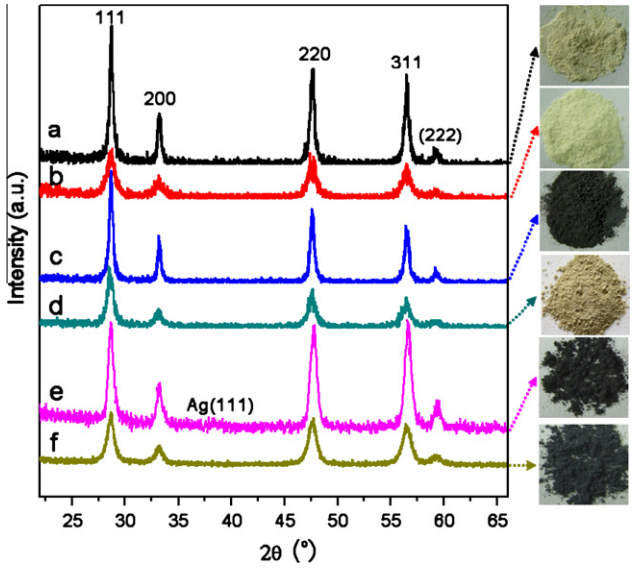

Fig. 2. XRD patterns and photographs of (a) *c*-CeO_2, (b) *r*-CeO_2, (c) 1%-Ag/*c*-CeO_2, (d) 1%-Ag/*r*-CeO_2, (e) 3%-Ag/*c*-CeO_2, and (f) 3%-Ag/*r*-CeO_2.

Table 1
Ag loadings, specific surface areas, and surface compositions of various samples.

Sample	Ag loading (wt%)	Specific surface area (m^2/g)
c-CeO_2		35.9
r-CeO_2		66.7
1%-Ag/*c*-CeO_2	0.76	33.2
1%-Ag/*r*-CeO_2	0.89	65.6
3%-Ag/*c*-CeO_2	2.47	27.9
3%-Ag/*r*-CeO_2	2.51	62.3

[44,45]; therefore, the average size of Ag nanoparticles in Ag/CeO_2 samples follows the order: 3%-Ag/*c*-CeO_2 > 1%-Ag/*c*-CeO_2 ≈ 3%-Ag/*r*-CeO_2.

XPS was employed to probe the structure of silver species in Ag/CeO_2 samples (Fig. 5). The Ag 3d XPS spectra of all samples are symmetric and with similar full-width at half-maximum (FWHM) of ~2.0 eV. 1%-Ag/*c*-CeO_2, 3%-Ag/*r*-CeO_2, and 3%-Ag/*c*-CeO_2 exhibit their Ag $3d_{5/2}$ binding energy at 368.4 eV that could be assigned to Ag nanoparticles supported on CeO_2 [38]; however, 1%-Ag/*r*-CeO_2 exhibit its Ag $3d_{5/2}$ binding energy at 367.6 eV. Due to the final state effect, positively charged silver species (Ag_n^+) exhibits a lower Ag $3d_{5/2}$ binding energy than metallic silver [46]. Therefore, positively charged Ag_n^+ species dominates in 1%-Ag/*r*-CeO_2, whereas metallic Ag nanoparticles dominate in 1%-Ag/*c*-CeO_2, 3%-Ag/*r*-CeO_2, and 3%-Ag/*c*-CeO_2. XAS was further employed to elucidate the nature of silver species in Ag/CeO_2 samples (Fig. 6). The reference samples, Ag foil, $AgNO_3$ powder and Ag_2O powder, display distinctly different Ag K-edge XANES spectra. The Ag K-edge XANES spectra of 1%-Ag/*c*-CeO_2 and 3%-Ag/*c*-CeO_2 are similar to that of Ag foil, evidencing the formation of metallic Ag nanoparticles. The features in the Ag K-edge XANES spectrum of 1%-Ag/*r*-CeO_2 are still similar to those of $AgNO_3$ powder, but impregnated $AgNO_3$ on *r*-CeO_2 should completely decompose after calcination at 500 °C. Similar experimental results were previously observed during the calcination process of $AgNO_3$-impregnated SiO_2 in which the formation of positively charged Ag_n^+ clusters were proposed [29]. Therefore, the dominating silver species in 1%-Ag/*r*-CeO_2 is positively charged Ag_n^+ clusters, agreeing with XPS results. The Ag K-edge XANES spectrum of 3%-Ag/*r*-CeO_2 mainly consists of the features arising from Ag foil, but the features of positively charged Ag_n^+ clusters are still visible. Thus, metallic Ag nanoparticles dominate in 3%-Ag/*r*-CeO_2, but positively charged Ag_n^+ clusters also exist.

Above structural characterizations clearly reveal that different silver species form in Ag/CeO_2 samples employed CeO_2 nanocubes and nanorods as the support. Fine Ag nanoparticles dominate 1%-Ag/*c*-CeO_2 and grow in size in 3%-Ag/*c*-CeO_2; however, positively charged Ag_n^+ clusters dominate in 1%-Ag/*r*-CeO_2, and fine Ag nanoparticles dominate in 3%-Ag/*r*-CeO_2. These results demonstrate that the interaction between silver and CeO_2 nanorods exposing {1 1 0} and {1 0 0} crystal planes is much stronger than that between silver and CeO_2 nanocubes exposing {1 0 0} crystal planes so that positively charged Ag_n^+ clusters could be stabilized on CeO_2 nanorodes but not on CeO_2 nanocubes when impregnated $AgNO_3$ thermally decomposed at 500 °C. It was previously observed that CeO_2 nanorods enclosed by {1 1 0} and {1 0 0} crystal planes are most active for gold stabilization/activation among CeO_2 nanorods, nanocubes, and nanopolyhedra [16]. The Ag–CeO_2 interaction not only affects the structure of silver species but also affects the concentration and structure of oxygen vacancies in CeO_2 support. Figs. 7 and 8 show Raman spectra of CeO_2 and Ag/CeO_2 excited by lasers with wavelengths of 514.5 (visible Raman) and 325 nm (UV Raman), respectively. Excited by 514.5 nm laser, both CeO_2 nanocubes and nanorods exhibit a strong peak at 465 cm^{-1} and two weak peaks at 598 and 1174 cm^{-1}, which correspond to the F_{2g}, defect-induced (D) and second-order longitudinal modes of cubic CeO_2 fluoride phase, respectively [47–49]. The Raman spectra of CeO_2 nanocubes and nanorods change in different ways after the loading of silver. For CeO_2 nanocubes, the F_{2g} and D bands, respectively, red-shift to 458 and 545 cm^{-1} after the loading of Ag nanoparticles; meanwhile, the D band obviously grows at the expense of the F_{2g} mode. For CeO_2 nanorods, the F_{2g} band red-shifts to 462 cm^{-1} in 1%-Ag/*r*-CeO_2 and further to 460 cm^{-1} in 3%-Ag/*r*-CeO_2, and the D band red-shifts to 590 cm^{-1} in 1%-Ag/*r*-CeO_2 and further to 579 cm^{-1} in 3%-Ag/*r*-CeO_2; meanwhile, the D band obviously grows at the expense of the F_{2g} mode in 3%-Ag/*r*-CeO_2. Excited by 325 nm laser, three peaks at 450, 587, and 1176 cm^{-1} that respectively correspond to the F_{2g}, D, and second-order longitudinal modes of cubic CeO_2 fluoride phase exhibit comparative intensities for both CeO_2 nanocubes and nanorods. After the loading of silver, these three bands do not shift, but their relative intensities of the bands change. We performed peaking fitting of the F_{2g} and defect-induced modes in the Raman spectra of various samples and calculated their ratio (I_D/I_{F2g}). The results are summarized in Table 2.

Above Raman spectra of CeO_2 and Ag/CeO_2 samples demonstrate several interesting results. Firstly, UV Raman gives much stronger defect-induced and second-order longitudinal modes of CeO_2 than visible Raman. This was observed previously and attributed to the resonance Raman effect [42,49,50] since CeO_2 strongly absorbs in the UV region. Secondly, after the loading of silver, the F_{2g} and D bands red-shift more or less in the visible Raman spectra but do not in the UV Raman spectra. Due to the much stronger absorption of both CeO_2 and Ag/CeO_2 in the UV light region than in the visible light region, UV Raman is more surface sensitive than visible Raman. The red-shift of D band to around 550 cm^{-1} was previously observed in doped and reduced CeO_2 and was associated with the creation of oxygen vacancies in CeO_2 [42,49,50]. These observations suggest that the loading of silver creates oxygen vacancies in the bulk region of CeO_2 rather than in the surface region; however, the loaded silver species should reasonably interact with the surface of CeO_2. This could be due to the argument that oxygen in the bulk of CeO_2 can migrate to the surface region to fill oxygen vacancies created by the Ag–CeO_2 interaction to some extents during the synthesis process, forming oxygen vacancies in the bulk region. Thirdly, after the loading of silver, the changes of I_D/I_{F2g} values are clearly shape-dependent. The I_D/I_{F2g}

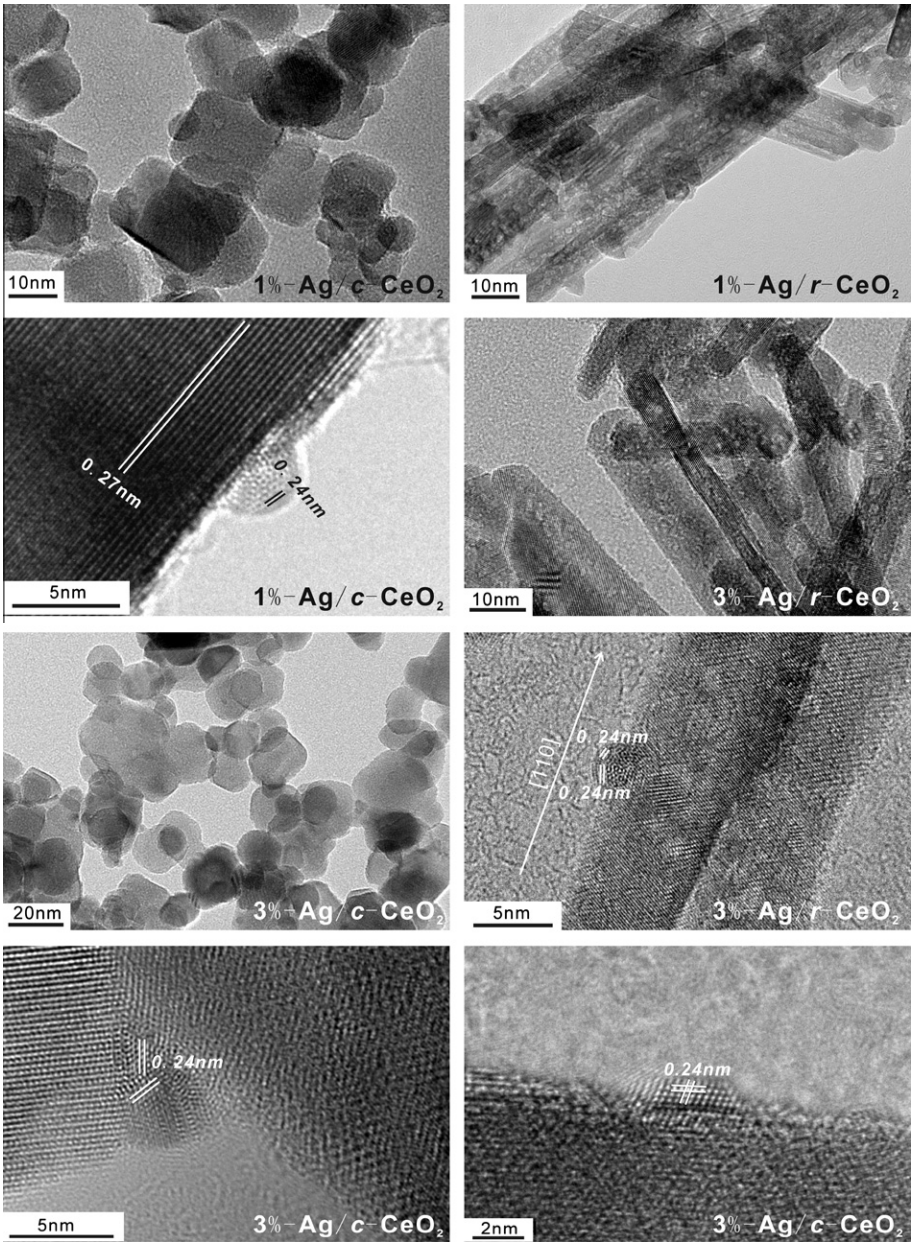

Fig. 3. TEM and HRTEM images of various samples.

values of both visible and UV Raman of CeO_2 nanorods are larger than those of CeO_2 nanocubes, indicating that CeO_2 nanorods have more oxygen vacancies than CeO_2 nanocubes. Wu et al. [42] also observed that CeO_2 nanorods have the most abundant oxygen vacancy sites, followed by CeO_2 nanocubes and nano-octahedra. Theoretical calculation studies show that the vacancies formation energy on different crystal planes CeO_2 follows the order of {1 1 0} < {1 0 0} < {1 1 1} [41]. After the loading of silver, the I_D/I_{F2g} value of visible Raman increases from 0.01 for *c*-CeO_2 dramatically to 1.15 for 1%-Ag/*c*-CeO_2 and then decreases to 0.79 for 3%-Ag/*c*-CeO_2, and that of UV Raman increases from 0.6 for *c*-CeO_2 to 1.39 for 1%-Ag/*c*-CeO_2 and further to 1.74 for 3%-Ag/*c*-CeO_2; meanwhile, the I_D/I_{F2g} value of visible Raman increases from 0.03 for *r*-CeO_2 slightly to 0.07 for 1%-Ag/*r*-CeO_2 and further to 0.25 for 3%-Ag/*r*-CeO_2, but that of UV Raman does not vary much among *r*-CeO_2, 1%-Ag/*r*-CeO_2, and 3%-Ag/*r*-CeO_2. Evidently, supported Ag nanoparticles are much more capable of creating oxygen vacancies in CeO_2 than supported positively charged Ag_n^+ clusters; meanwhile, much more oxygen vacancies form in Ag/*c*-CeO_2 than in Ag/*r*-CeO_2 although *r*-CeO_2 has more oxygen vacancies than *c*-CeO_2. This for the first time demonstrates that the formation of oxygen vacancies in CeO_2 nanocrystals induced by the Ag–CeO_2 interaction depends on the crystal planes exposed by CeO_2 nanocrystals. It is noteworthy that the order of oxygen vacancy formation between CeO_2 nanocubes and nanorods in Ag/CeO_2 catalysts is opposite to that in pure CeO_2 nanocrystals. This clearly demonstrates that the Ag–CeO_2 interaction exerts great influences on the structure of CeO_2 nanocrystals.

PALS, a well-established technique to study defects in materials [21,50–55], was employed to further probe the structure of oxygen vacancies in various samples. Fig. 9 displays PALS spectra that were peak-fitted with three components. The results were summarized in Table 2 (τ, lifetime of the positron; *I*, corresponding intensity). The lifetime of positrons is determined by the average electron density at the annihilation site, and it increases with the decrease of the average electron density [54]. The component with longest lifetime

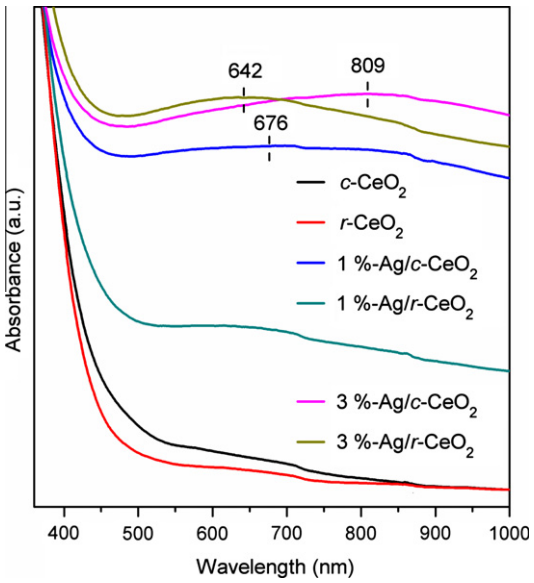

Fig. 4. UV–Vis diffuse reflectance spectra of various samples.

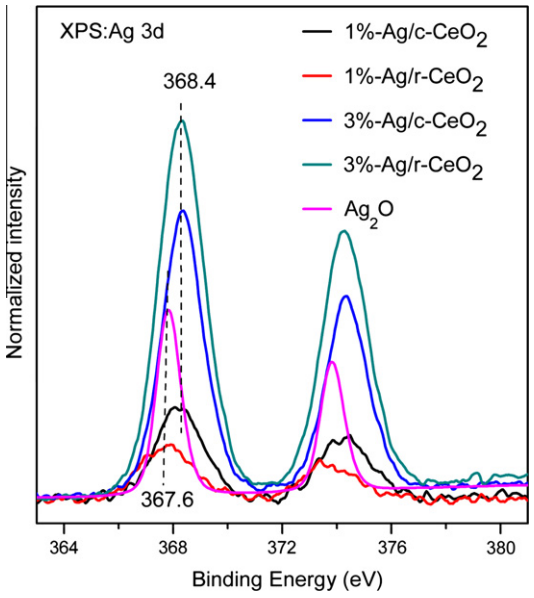

Fig. 5. Ag 3d XPS spectra of various samples.

τ_3 is generally due to the annihilation of ortho-positronium atoms in the large voids in the material whose formation is a separate physical process not related to positron trapping at defects [50,51]. CeO_2 nanocubes exhibit two components with the lifetime of 187 (τ_1) and 350.2 ps (τ_2). The τ_1 and τ_2 components respectively correspond to the free annihilation of positrons in CeO_2 and the annihilation of positrons in large oxygen vacancy clusters in CeO_2 [21,52,53]. CeO_2 nanorods exhibit two components with the lifetime of 262 (τ_1) and 397 ps (τ_2). The τ_2 component corresponds to the annihilation of positrons in large oxygen vacancy clusters in CeO_2 while the τ_1 component arises from the annihilation of positrons in small oxygen vacancies in CeO_2 such as Ce^{3+}-oxygen vacancy associates and mono-vacancies [21,52,53]. Therefore, PALS results demonstrate that CeO_2 nanocubes and nanorods are with different structures of oxygen vacancies. CeO_2 nanocubes are mainly with large oxygen vacancy clusters while CeO_2 nanorods

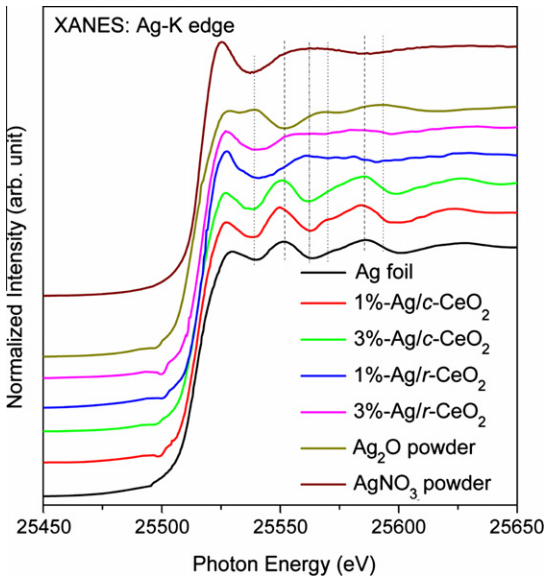

Fig. 6. Ag K-edge XANES spectra of various samples.

are with both small oxygen vacancies and large oxygen vacancy clusters. Meanwhile, oxygen vacancy clusters in CeO_2 nanorods are with a lower average electron density than those in CeO_2 nanocubes.

The life times of two components of 1%-Ag/*c*-CeO_2 are 203.3 (τ_1) and 366.1 ps (τ_2), and those of 3%-Ag/*c*-CeO_2 are 198.9 (τ_1) and 360.7 ps (τ_2). These values are all larger than the corresponding values of CeO_2 nanocubes. Thus, the loading of Ag nanoparticles on CeO_2 nanocubes leads to the formation of small oxygen vacancies and the decrease of the average electron density of oxygen vacancy clusters. The latter might be attributed to the increase in the size of oxygen vacancy clusters after CeO_2 nanocubes are loaded with Ag nanoparticles. The I_2/I_1 ratio decreases from 1.75 for CeO_2 nanocubes to 1.32 for 1%-Ag/*c*-CeO_2 and 1.44 for 3%-Ag/*c*-CeO_2.

Interestingly, 1%-Ag/*r*-CeO_2 exhibits two components whose life times (230.2 and 384.7 ps) are shorter than the corresponding values of CeO_2 nanorods, indicating that both small oxygen vacancies and oxygen vacancy clusters in 1%-Ag/*r*-CeO_2 have the higher average electron density than those in CeO_2 nanorods. Positively charged Ag_n^+ clusters dominate in 1%-Ag/*r*-CeO_2, thus oxygen vacancies in 1%-Ag/*r*-CeO_2 might bear extra charge for the charge balance and are thus with the higher average charge density than oxygen vacancies in CeO_2 nanorods. 3%-Ag/*r*-CeO_2 exhibits two components with the life time of 250.2 (τ_1) and 409.3 ps (τ_2). Its τ_1 is longer than that of 1%-Ag/*r*-CeO_2 but still shorter than that of CeO_2 nanorods, and its τ_2 is longer than that of CeO_2 nanorods. Ag nanoparticles dominate in 3%-Ag/*r*-CeO_2 but positively charged Ag_n^+ clusters also exist. Ag nanoparticles are associated with large oxygen vacancy clusters in 3%-Ag/*r*-CeO_2. Similar to the case in Ag/*c*-CeO_2, oxygen vacancy clusters are larger in 3%-Ag/*r*-CeO_2 than in CeO_2 nanorods and thus exhibit the lower average electron density. Positively charged Ag_n^+ clusters mainly interact with small oxygen vacancies in 3%-Ag/*r*-CeO_2 that thus still exhibits the higher average electron density than those in CeO_2 nanorods. It is also interesting that the I_2/I_1 ratio increases from 2.18 for CeO_2 nanorods to 3.55 for 1%-Ag/*r*-CeO_2 with positively charged Ag_n^+ clusters, but then decreases to 1.39 for 3%-Ag/*r*-CeO_2 with dominant Ag nanoparticles that is similar to the I_2/I_1 ratio for Ag/*c*-CeO_2 with Ag nanoparticles.

Above structural characterization results for the first time reveal the shape-dependent interplay between oxygen vacancies and Ag–CeO_2 interaction in Ag/CeO_2 samples. CeO_2 nanorods enclosed with

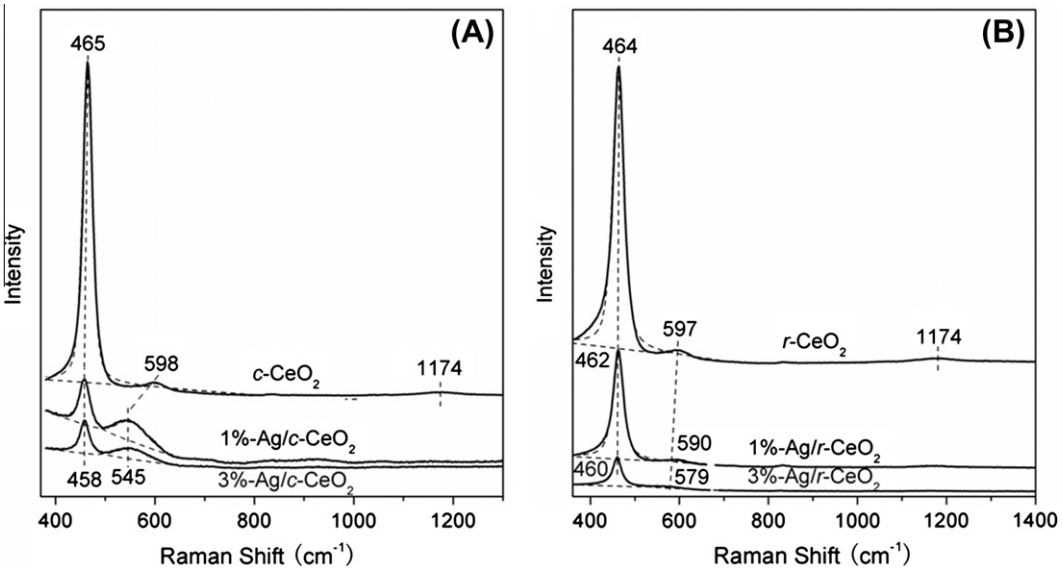

Fig. 7. Visible Raman spectra of (A) c-CeO_2, 1%-Ag/c-CeO_2, 3%-Ag/c-CeO_2, and (B) r-CeO_2, 1%-Ag/r-CeO_2, 3%-Ag/r-CeO_2.

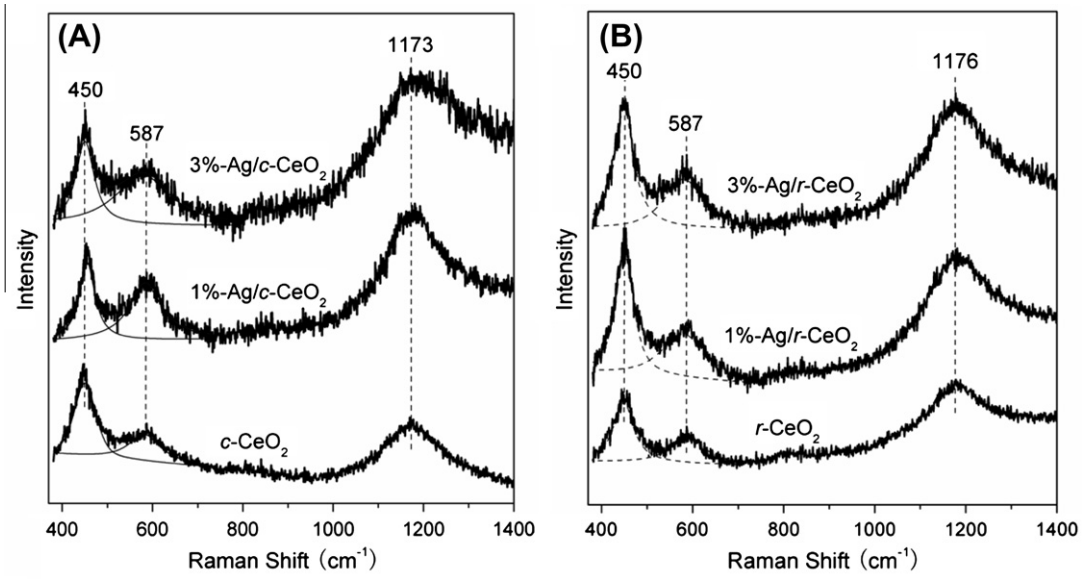

Fig. 8. UV Raman spectra of (A) c-CeO_2, 1%-Ag/c-CeO_2, 3%-Ag/c-CeO_2, and (B) r-CeO_2, 1%-Ag/r-CeO_2, 3%-Ag/r-CeO_2.

Table 2
Peak-fitting results of PALS spectra and Raman spectra of various samples.

Sample	PALS spectra							Raman spectra	
	τ_1 (ps)	τ_2 (ps)	τ_3 (ns)	I_1 (%)	I_2 (%)	I_3 (%)	I_2/I_1	I_D/I_{F2g}	
								325 nm	541.5 nm
c-CeO_2	187.0	350.2	1.50	35.99	63.16	0.85	1.75	0.60	0.01
1%-Ag/c-CeO_2	203.3	366.1	2.10	42.82	56.48	0.70	1.32	1.39	1.15
3%-Ag/c-CeO_2	198.9	360.7	1.74	40.6	58.5	0.9	1.44	1.74	0.79
r-CeO_2	262.0	397.0	1.90	31.2	67.9	0.9	2.18	0.76	0.03
1%-Ag/r-CeO_2	230.2	384.7	1.71	21.72	77.06	1.22	3.55	0.89	0.07
3%-Ag/r-CeO_2	250.2	409.3	2.36	41.5	57.5	1.0	1.39	0.77	0.25

{110} and {100} crystal planes are with a slightly higher oxygen vacancy concentration than CeO_2 nanocubes enclosed with {100} crystal planes, and CeO_2 nanorods are with both small oxygen vacancies and large oxygen vacancy clusters while CeO_2 nanocubes are mainly with large oxygen vacancy clusters. When employed as the support to prepare Ag/CeO_2 catalysts, CeO_2 nanocubes and nanorods exhibit different Ag–CeO_2 interactions, not only forming different silver species but also exerting different influences on

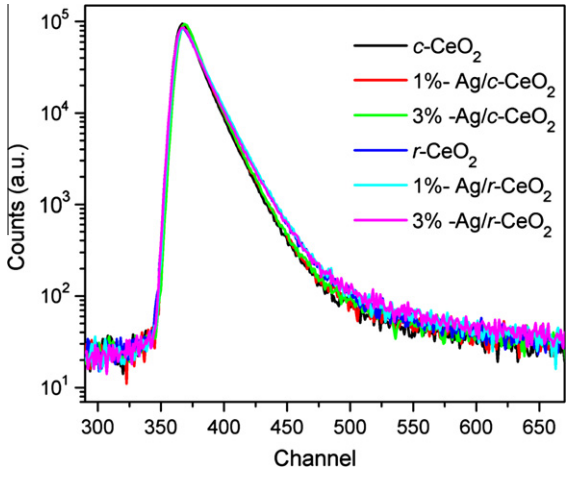

Fig. 9. Positron annihilation lifetime spectra of various samples.

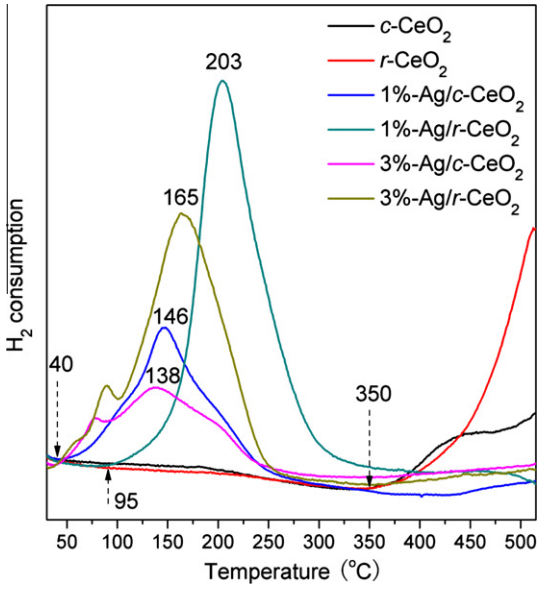

Fig. 10. H_2-TPR profiles of various samples.

their oxygen vacancies. Fine Ag nanoparticles form in 1%-Ag/*c*-CeO_2 and grow in size in 3%-Ag/*c*-CeO_2; however, positively charged Ag_n^+ clusters dominate in 1%-Ag/*r*-CeO_2, and fine Ag nanoparticles dominate in 3%-Ag/*r*-CeO_2. More oxygen vacancies form in Ag/*c*-CeO_2 than in Ag/*r*-CeO_2. Supported Ag nanoparticles are much more capable of creating oxygen vacancies in CeO_2 than supported positively charged silver clusters. The average charge density of oxygen vacancies and the ratio between large oxygen vacancy clusters and small vacancies in CeO_2 nanocrystals are enhanced with supported positively charged Ag_n^+ clusters but reduced with supported Ag nanoparticles.

Oxygen vacancies play a decisive role in the surface reactivity and catalytic performance of CeO_2 nanoparticles. Fig. 10 displays H_2-TPR spectra of various samples. The surface reduction peak of CeO_2 nanorods is larger than that of CeO_2 nanocubes, which could be associated with the difference of specific surface area between CeO_2 nanocubes (35.9 m^2/g) and nanorods (66.7 m^2/g) (Table 1). However, the surface reduction of CeO_2 nanocubes and nanorods initiates at the similar temperature (350 °C), which could be attributed to the fact that CeO_2 nanorods are only with a slightly higher oxygen vacancy concentration than CeO_2 nanocubes. Interestingly, 1%-Ag/*c*-CeO_2, 3%-Ag/*c*-CeO_2, and 3%-Ag/*r*-CeO_2 exhibit their surface reduction at the same temperature (40 °C) with the peak maximum at 146, 138, and 165 °C, respectively. This can be well explained similar silver and oxygen vacancy structures of 1%-Ag/*c*-CeO_2, 3%-Ag/*c*-CeO_2, and 3%-Ag/*r*-CeO_2: Ag nanoparticles, high oxygen vacancy concentrations, and similar ratios between large oxygen vacancy clusters and small vacancies. Ag nanoparticles activate surface lattice oxygen in CeO_2 and facilely dissociate H_2, greatly facilitating the surface reduction of CeO_2 nanocrystals at low temperatures. 1%-Ag/*r*-CeO_2 with positively charged Ag_n^+ clusters gets reduced at 95 °C with the peak maximum at 203 °C. It is very likely that positively charged Ag_n^+ clusters in 1%-Ag/*r*-CeO_2 are firstly reduced into Ag nanoparticles, subsequently promoting the surface reduction of CeO_2. Therefore, Ag nanoparticles greatly promote the reduction of CeO_2 nanocrystals but positively charged Ag_n^+ clusters do not.

Fig. 11A shows CO conversion as a function of reaction temperature of various catalysts in CO oxidation. CeO_2 nanocubes become active at 210 °C and CeO_2 nanorods are slightly active than CeO_2 nanocubes, which could be associated with their specific surface areas. The catalytic performances of Ag/CeO_2 catalysts are better than CeO_2 nanocrystals, but vary with their structures of silver and oxygen vacancies. 1%-Ag/*r*-CeO_2 with positively charged Ag_n^+ clusters becomes active above 120 °C but only achieves a 80% CO conversion at 300 °C. 1%-Ag/*c*-CeO_2 with Ag nanoparticles is very active, becoming active above 60 °C and achieving a 100% CO conversion at 195 °C. With higher loadings of Ag nanoparticles, 3%-Ag/*c*-CeO_2 and 3%-Ag/*r*-CeO_2 are more catalytically active than 1%-Ag/*c*-CeO_2 and achieve a 100% CO conversion at 165 °C. The catalytic performances of various CeO_2 and Ag/CeO_2 catalysts are in line with their reducibility, indicating that surface lattice oxygen in CeO_2 participates into catalytic CO oxidation. With this respect, CeO_2 with a high oxygen vacancy concentration and appropriate ratios between large oxygen vacancy clusters and small vacancies are catalytically active. We have also calculated the corresponding turn-over frequency (TOF) of various Ag/CeO_2 catalysts with respect to the Ag loading in CO oxidation (Fig. 11B). The TOF values of our catalysts are lower than those of Ag/CeO_2 composite catalysts prepared by co-precipitation method [24].

Surface lattice oxygen and oxygen vacancies are always involved in oxidation reactions catalyzed by CeO_2-based catalysts; therefore, tuning the reactivity of surface lattice oxygen and the oxygen vacancy structure in CeO_2 is the key to optimize the catalytic activity, which can be achieved via the loading of noble metals. Our results demonstrate that different structures of supported noble metals exert different influences on the oxygen vacancy structure of CeO_2. Supported Ag nanoparticles are much more capable of activating the surface lattice oxygen, creating oxygen vacancies, promoting the surface reduction, and catalytic activity of CeO_2 than supported Ag_n^+ clusters. More importantly, our results demonstrate that, under the same preparation procedure, the structure of silver supported on CeO_2 is controlled by the shape of CeO_2 via the shape-dependent interplay between oxygen vacancies and Ag–CeO_2 interaction. CeO_2 nanorods enclosed with {1 1 0} and {1 0 0} crystal planes and CeO_2 nanocubes enclosed with {1 0 0} crystal planes are with different concentrations and structures of oxygen vacancies, and CeO_2 nanorods exhibit the stronger silver–CeO_2 interaction than CeO_2 nanocubes. On one hand, these results demonstrate that the interplay between oxygen vacancies and Ag–CeO_2 interaction controls the structures of silver and CeO_2 in Ag/CeO_2 catalysts and thus their catalytic activity, deepening the fundamental understanding of metal/CeO_2 catalysts. On the other hand, these results reveal that the interplay between oxygen vacancies and Ag–CeO_2 interaction depends on the shape of CeO_2 support, opening up a new strategy for the design of efficient and economic metal/CeO_2 catalysts by engineering the shape of

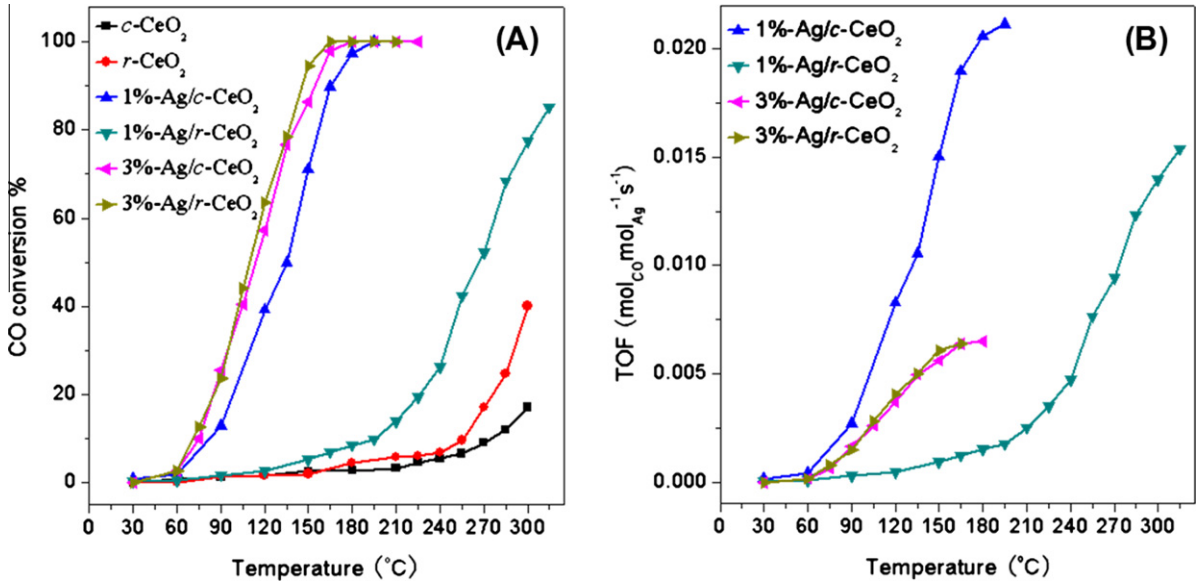

Fig. 11. (A) CO conversion as a function of reaction temperature of various CeO_2 and Ag/CeO_2 catalysts in CO oxidation and (B) corresponding turn-over frequency calculated with respect to the Ag loading of various.

CeO_2 support. Ag nanoparticles and CeO_2 with a high oxygen vacancy concentration and appropriate ratios between large oxygen vacancy clusters and small vacancies compose the active structure in catalyzing CO oxidation; therefore, CeO_2 nanocubes are better than CeO_2 nanorods as the support to prepare Ag/CeO_2 catalysts with a low silver loading but a high catalytic activity.

4. Conclusions

Employing CeO_2 nanocubes and nanorods as the support, we have successfully revealed the shape-dependent interplay between oxygen vacancies and Ag–CeO_2 interaction in Ag/CeO_2 catalysts and the active structure of Ag/CeO_2 catalysts in CO oxidation:

(1) CeO_2 nanocrystals with different shapes are with different concentrations and structures of oxygen vacancies. CeO_2 nanorods enclosed with {110} and {100} crystal planes are with a higher oxygen vacancy concentration than CeO_2 nanocubes enclosed with {100} crystal planes, and CeO_2 nanorods are with both small oxygen vacancies and large oxygen vacancy clusters while CeO_2 nanocubes are mainly with large oxygen vacancy clusters.

(2) The concentration and structure of oxygen vacancies in CeO_2 determine the metal–CeO_2 interaction and the structure of supported metal in metal/CeO_2 catalysts. CeO_2 nanorods exhibit the stronger silver–CeO_2 interaction than CeO_2 nanocubes. Positively charged Ag_n^+ clusters dominate in 1%-Ag/r-CeO_2, and fine Ag nanoparticles dominate in 3%-Ag/r-CeO_2; however, fine Ag nanoparticles form in 1%-Ag/c-CeO_2 and grow in size in 3%-Ag/c-CeO_2.

(3) Supported noble metals with different structures exert different influences on the concentration and structure of oxygen vacancies in CeO_2 of metal/CeO_2 catalysts. Supported Ag nanoparticles are much more capable of activating the surface lattice oxygen, creating oxygen vacancies, and promoting the surface reduction of CeO_2 than supported Ag_n^+ clusters in Ag/CeO_2 catalysts. The average charge density of oxygen vacancies and the ratio between large oxygen vacancy clusters and small vacancies in CeO_2 nanocrystals are enhanced with supported positively charged Ag_n^+ clusters but reduced with supported Ag nanoparticles.

(4) Ag nanoparticles and CeO_2 with a high oxygen vacancy concentration and appropriate ratios between large oxygen vacancy clusters and small vacancies compose the active structure in catalyzing CO oxidation. CeO_2 nanocubes are a better support than CeO_2 nanorods to prepare Ag/CeO_2 catalysts with a low silver loading but a high catalytic activity.

These conclusions not only deepen the fundamental understanding of metal/CeO_2 catalysts, but also open up a new strategy for the design of efficient and economic metal/CeO_2 catalysts by engineering the shape of CeO_2 support.

Acknowledgments

This work was financially supported by National Natural Science Foundation of China(Grant 21173204 and J1030412), National Basic Research Program of China, the Fundamental Research Funds for the Central Universities. and the MPG-CAS partner group program. We gratefully acknowledge Dr. Zheng Jiang, Prof. Yuying Huang, and Dr. Shuo Zhang at Shanghai Synchrotron Radiation Facility for their assistance in the XAS experiments.

References

[1] J.A. van Bokhoven, ChemCatChem 1 (2009) 363–364.
[2] B.M. Choudary, R.S. Mulukutla, K.J. Klabunde, J. Am. Chem. Soc. 125 (2003) 2020–2021.
[3] L.H. Hu, Q. Peng, Y.D. Li, J. Am. Chem. Soc. 130 (2008) 16136–16137.
[4] X.W. Xie, Y. Li, Z.Q. Liu, M. Haruta, W.J. Shen, Nature 458 (2009) 746–749.
[5] H.Z. Bao, W.H. Zhang, D.L. Shang, Q. Hua, Y.S. Ma, Z.Q. Jiang, J.L. Yang, W.X. Huang, J. Phys. Chem. C 114 (2010) 6676–6680.
[6] Q. Hua, D.L. Shang, W.H. Zhang, K. Chen, S.J. Chang, Y.S. Ma, Z.Q. Jiang, J.L. Yang, W.X. Huang, Langmuir 27 (2010) 665–671.
[7] H.Z. Bao, W.H. Zhang, Q. Hua, Z.Q. Jiang, J.L. Yang, W.X. Huang, Angew. Chem. Int. Ed. 123 (2011) 12502–12506.
[8] Q. Hua, K. Chen, S.J. Chang, Y.S. Ma, W.X. Huang, J. Phys. Chem. C 115 (2011) 20618–20627.
[9] A. Trovarelli, Catal. Rev. –Sci. Eng. 38 (1996) 439–520.
[10] A. Trovarelli, Catalysis by Ceria and Related Materials, Imperial College Press, London, 2002.
[11] S. Carrettin, P. Concepción, A. Corma, J.M. López Nieto, V.F. Puntes, Angew. Chem. Int. Ed. 43 (2004) 2538–2540.
[12] K.B. Zhou, X. Wang, X.M. Sun, Q. Peng, Y.D. Li, J. Catal. 229 (2005) 206–212.
[13] H.X. Mai, L.D. Sun, Y.W. Zhang, R. Si, W. Feng, H.P. Zhang, H.C. Liu, C.H. Yan, J. Phys. Chem. B 109 (2005) 24380–24385.
[14] W.Q. Han, L.J. Wu, Y.M. Zhu, J. Am. Chem. Soc. 127 (2005) 12814–12815.

[15] K.B. Zhou, Z.Q. Yang, S. Yang, Chem. Mater. 19 (2007) 1215–1217.
[16] R. Si, M. Flytzani-Stephanopoulos, Angew. Chem. Int. Ed. 47 (2008) 2884–2887.
[17] M.L. Tana, J. Zhang, H.J. Li, Y. Li, W.J. Li, Shen, Catal. Today 148 (2009) 179–183.
[18] Y. Guan, E.J.M. Hensen, Phys. Chem. Chem. Phys. 11 (2009) 9578–9582.
[19] L. Feng, D.T. Hoang, C.K. Tsung, W.Y. Huang, S.H.Y. Lo, J.B. Wood, H.T. Wang, J.Y. Tang, P.D. Yang, Nano Research 4 (2011) 61–71.
[20] Y. Guan, D. Ligthart, Ö. Pirgon-Galin, J. Pieterse, R. van Santen, E. Hensen, Top. Catal. 54 (2011) 424–438.
[21] X.W. Liu, K.B. Zhou, L. Wang, B.Y. Wang, Y.D. Li, J. Am. Chem. Soc. 131 (2009) 3140–3141.
[22] Z.L. Wu, M.J. Li, S.H. Overbury, J. Catal. 285 (2012) 61–73.
[23] L. Kundakovic, M. Flytzani-Stephanopoulos, J. Catal. 179 (1998) 203–221.
[24] S. Imamura, H. Yamada, K. Utani, Appl. Catal. A 192 (2000) 221–226.
[25] Q. Fu, H. Saltsburg, M. Flytzani-Stephanopoulos, Science 301 (2003) 935–938.
[26] X.F. Tang, J.L. Chen, Y.G. Li, Y. Li, Y.D. Xu, W.J. Shen, Chem. Eng. J. 118 (2006) 119–125.
[27] W.J. Cai, F.G. Wang, A.C. Van Veen, H. Provendier, C. Mirodatos, W.J. Shen, Catal. Today 138 (2008) 152–156.
[28] M. Hatanaka, N. Takahashi, N. Takahashi, T. Tanabe, Y. Nagai, A. Suda, H. Shinjoh, J. Catal. 266 (2009) 182–190.
[29] M.J. Beier, T.W. Hansen, J.D. Grunwaldt, J. Catal. 266 (2009) 320–330.
[30] H.P. Zhou, H.S. Wu, J. Shen, A.X. Yin, L.D. Sun, C.H. Yan, J. Am. Chem. Soc. 132 (2010) 4998–4999.
[31] T. Kayama, K. Yamazaki, H. Shinjoh, J. Am. Chem. Soc. 132 (2010) 13154–13155.
[32] A. Primo, T. Marino, A. Corma, R. Molinari, H. García, J. Am. Chem. Soc. 133 (2011) 6930–6933.
[33] M.J. Li, Z.L. Wu, S.H. Overbury, J. Catal. 278 (2011) 133–142.
[34] C.M. Kalamaras, S. Americanou, A.M. Efstathiou, J. Catal. 279 (2011) 287–300.
[35] T.X.T. Sayle, S.C. Parker, C.R.A. Catlow, Surf. Sci. 316 (1994) 329–336.
[36] C.T. Campbell, J.A. Farmer, Science 329 (2010) 933–936.
[37] J.A. Farmer, J.H. Baricuatro, C.T. Campbell, J. Phys. Chem. C 114 (2010) 17166–17172.
[38] D.D. Kong, G.D. Wang, Y.H. Pan, S.W. Hu, J.B. Hou, H.B. Pan, C.T. Campbell, J.F. Zhu, J. Phys. Chem. C 115 (2011) 6715–6725.
[39] F. Esch, S. Fabris, L. Zhou, T. Montini, C. Africh, P. Fornasiero, G. Comelli, R. Rosei, Science 309 (2005) 752–755.
[40] C.T. Campbell, C.H.F. Peden, Science 309 (2005) 713–714.
[41] M. Nolan, S.C. Parker, G.W. Watson, Surf. Sci. 595 (2005) 223–232.
[42] Z. Wu, M. Li, J. Howe, H.M. Meyer, S.H. Overbury, Langmuir 26 (2010) 16595–16606.
[43] S.T. Oyama, X. Zhang, J. Lu, Y. Gu, T. Fujitana, J. Catal. 257 (2008) 1–4.
[44] H. Zhang, G. Wang, D. Chen, X.J. Lv, U.H. Jinghong, Chem. Mater. 20 (2008) 6543–6549.
[45] W. Sun, Y.Z. Li, W.Q. Shi, X.J. Zhao, P.F. Fang, J. Mater. Chem. 21 (2011) 9263–9270.
[46] T.F. Moulder, W.J. Stickle, P.E. Sobol, K.D. Bomben, Handbook of X-ray Photoelectron Spectroscopy, Perkin Elmer, Eden Prairie, Minnesota, 1992.
[47] W.H. Weber, K.C. Hass, J.R. McBride, Phys. Rev. B 48 (1993) 178–185.
[48] A. Nakajima, A. Yoshihara, M. Ishigame, Phys. Rev. B 50 (1994) 13297–13307.
[49] T. Taniguchi, T. Watanabe, N. Sugiyama, A.K. Subramani, H. Wagata, N. Matsushita, M. Yoshimura, J. Phys. Chem. C 113 (2009) 19789–19793.
[50] M.F. Luo, Z.L. Yan, L.Y. Jin, M. He, J. Phys. Chem. B 110 (2006) 13068.
[51] S. Dutta, S. Chattopadhyay, D. Jana, A. Banerjee, S. Manik, S.K. Pradhan, M. Sutradhar, A. Sarkar, J. Appl. Phys. 100 (2006) 114328.
[52] A. Sachdeva, S.V. Chavan, A. Goswami, A.K. Tyagi, P.K. Pujari, J. Solid State Chem. 178 (2005) 2062–2066.
[53] S. Ohta, T. Kosaka, K. Sato, in: Advanced Science Research Symposium 2009, Positron, Muon and Other Exotic Particle Beams for Materials and Atomic/Molecular Sciences, vol. 225, 2010.
[54] M.J. Puska, R.M. Nieminen, Rev. Mod. Phys. 66 (1994) 841–897.
[55] M. Kong, Y.Z. Li, X. Chen, T.T. Tian, P.F. Fang, F. Zheng, X.J. Zhao, J. Am. Chem. Soc. 133 (2011) 16414–16417.